The Astrophysical Journal, 941:114 (11pp), 2022 December 20 https://doi.org/10.3847/1538-4357/aca08b
© 2022. The Author(s). Published by the American Astronomical Society.
OPEN ACCESS

The Cavity of 3CR 196.1: Hα Emission Spatially Associated with an X-Ray Cavity

A. Jimenez-Gallardo[1,2,3,4], E. Sani[2], F. Ricci[5,6], C. Mazzucchelli[2,7], B. Balmaverde[3], F. Massaro[1,3,8,9], A. Capetti[3], W. R. Forman[10], R. P. Kraft[10], G. Venturi[11,12], M. Gendron-Marsolais[2,13], M. A. Prieto[14,15], A. Marconi[12,16], H. A. Peña-Herazo[17], S. A. Baum[18], C. P. O'Dea[18], L. Lovisari[5], R. Gilli[5], E. Torresi[5], A. Paggi[1,3,8], V. Missaglia[1,3,8], G. R. Tremblay[10], and B. J. Wilkes[10]

[1] Dipartimento di Fisica, Università degli Studi di Torino, via Pietro Giuria 1, I-10125 Torino, Italy; ana.jimenezgallardo@unibo.it
[2] European Southern Observatory, Alonso de Córdova 3107, Vitacura, Región Metropolitana, Chile
[3] INAF-Osservatorio Astrofisico di Torino, via Osservatorio 20, I-10025 Pino Torinese, Italy
[4] Dipartimento di Fisica e Astronomia dell'Università degli Studi di Bologna, via P. Gobetti 93/2, I-40129 Bologna, Italy
[5] INAF- Osservatorio di Astrofisica e Scienza dello Spazio di Bologna, via Gobetti 93/3, I-40129 Bologna, Italy
[6] Dipartimento di Matematica e Fisica, Universitá Roma Tre, Via della Vasca Navale 84, 00146, Roma, Italy
[7] Núcleo de Astronomía, Facultad de Ingeniería y Ciencias, Universidad Diego Portales, Av. Ejército 441, Santiago, 8320000, Chile
[8] Istituto Nazionale di Fisica Nucleare, Sezione di Torino, I-10125 Torino, Italy
[9] Consorzio Interuniversitario per la Fisica Spaziale, via Pietro Giuria 1, I-10125 Torino, Italy
[10] Center for Astrophysics | Harvard & Smithsonian, 60 Garden Street, Cambridge, MA 02138, USA
[11] Instituto de Astrofísica, Facultad de Física, Pontificia Universidad Católica de Chile, Casilla 306, Santiago 22, Chile
[12] INAF—Osservatorio Astrofisico di Arcetri, Largo E. Fermi 5, I-50125 Firenze, Italy
[13] Instituto de Astrofísica de Andalucía (IAA-CSIC), Glorieta de la Astronomía, E-18008 Granada, Spain
[14] Departamento de Astrofísica, Universidad de La Laguna, E-38206 La Laguna, Tenerife, Spain
[15] Instituto de Astrofísica de Canarias (IAC), E-38200 La Laguna, Tenerife, Spain
[16] Dipartimento di Fisica e Astronomia, Università di Firenze, via G. Sansone 1, I-50019 Sesto F.no, Firenze, Italy
[17] East Asian Observatory, 660 North A'ohōkū Place, Hilo, HI 96720, USA
[18] University of Manitoba, Dept. of Physics and Astronomy, Winnipeg, MB R3T 2N2, Canada
Received 2022 January 5; revised 2022 September 28; accepted 2022 November 3; published 2022 December 15

Abstract

We present a multifrequency analysis of the radio galaxy 3CR 196.1 (z=0.198), associated with the brightest galaxy of the cool-core cluster CIZAJ0815.4-0303. This nearby radio galaxy shows a hybrid radio morphology and an X-ray cavity, all signatures of a turbulent past activity, potentially due to merger events and active galactic nuclei (AGN) outbursts. We present results of the comparison between Chandra and Very Large Telescope Multi-Unit Spectroscopic Explorer data for the inner region of the galaxy cluster, on a scale of tens of kpc. We discovered Hα + [N II]λ6584 emission spatially associated with the X-ray cavity (at ∼10 kpc from the galaxy nucleus) instead of with its rim. This result differs from previous discoveries of ionized gas surrounding X-ray cavities in other radio galaxies harbored in galaxy clusters and could represent the first reported case of ionized gas filling an X-ray cavity, either due to different AGN outbursts or to the cooling of warm ($10^4 < T \leqslant 10^7$ K) AGN outflows. We also found that the Hα, [N II]λλ6548, 6584, and [S II]λλ6718, 6733 emission lines show an additional redward component, at ∼1000 km s^{-1} from rest frame, with no detection in Hβ or [O III]λλ4960, 5008. We believe the most likely explanation for this redward component is the presence of a background gas cloud as there appears to be a discrete difference of velocities between this component and the rest frame.

Unified Astronomy Thesaurus concepts: Active galactic nuclei (16); Radio active galactic nuclei (2134); Galaxy clusters (584); Cool cores (302)

1. Introduction

The extragalactic fraction of the Third Cambridge Catalog of radio sources and its revised versions (3C, 3CR, 3CRR, Edge et al. 1959; Bennett & Simth 1962; Laing et al. 1983; Spinrad et al. 1985) constitute one of the most valuable samples of powerful radio-loud active galactic nuclei (AGN) to explore feedback processes occurring between radio galaxies and their environments (see, e.g., McNamara & Nulsen 2007; Fabian 2012; McNamara & Nulsen 2012 and Kraft et al. (2012)).

One of the main pieces of evidence of radio mode feedback occurring in AGN in galaxy clusters and groups is the presence of X-ray cavities, first reported by Böhringer et al. (1996) and Churazov et al. (2000), due to the interaction of jets with the intracluster medium (ICM; see reviews by McNamara & Nulsen (2007), Fabian (2012), and Gitti et al. (2012); and works by Bîrzan et al. (2004), Cavagnolo et al. (2010), and McNamara & Nulsen (2012)). Some of the most remarkable examples of cavities include those of Perseus (see Fabian et al. 2003, 2006 and Graham et al. 2008), M87 (see, e.g., Forman et al. 2005, 2017), Hydra A (Nulsen et al. 2005a), Hercules A (Nulsen et al. 2005b), MS0735.6 + 7421 (McNamara et al. 2005, 2009), NGC 5813 (Randall et al. 2011, 2015), A2052 (Blanton et al. 2011), A2597 (Tremblay et al. 2012), and NGC 4636 (Jones et al. 2002).

Although it is common to find Hα emission either surrounding X-ray cavities (see, e.g., Blanton et al. 2011; Tremblay et al. 2015; Balmaverde et al. 2018), or spatially associated with radio emission (known as the "alignment effect"; see, e.g., Fosbury 1986; Hansen et al. 1987; Baum et al. 1988; McCarthy 1988; Baum et al. 1990; Tremblay et al. 2009; Baldi et al. 2019), the effect of radio jets on extended emission line regions (EELR,

Original content from this work may be used under the terms of the Creative Commons Attribution 4.0 licence. Any further distribution of this work must maintain attribution to the author(s) and the title of the work, journal citation and DOI.

regions of line-emitting gas on scales of tens of kpc; see, e.g., Baum et al. 1988) is not yet fully understood.

A recent analysis of radio, optical, and X-ray emission in 3CR 196.1 showed it is a promising source to investigate how radio jets affect EELRs, thanks to the discovery of an X-ray cavity at ∼10 kpc from the nucleus toward the southwest (see Ricci et al. 2018). Moreover, recent observations from the Multi-Unit Spectroscopic Explorer (MUSE; Bacon et al. 2010) at the Very Large Telescope (VLT) obtained as part of the MUse RAdio Loud Emission line Snapshot (MURALES) survey (Balmaverde et al. 2021) revealed that the Hα + [N II]λ6584 emission extends beyond the radio emission and appears, in projection, spatially associated with the X-ray cavity.

To test where such optical emission stands with respect to the X-rays, we compared the optical, X-ray, and radio emission of 3CR 196.1 up to a few tens of kpc, taking advantage of new VLT/MUSE observations. This emission had not been detected in previous Hubble Space Telescope (HST) data originally published in Tremblay et al. (2009), due to HST's lower sensitivity compared to MUSE. This spatial association of ionized gas with an X-ray cavity, instead of with its borders has been rarely reported in the literature (see, e.g., A1668; Pasini et al. 2021). We focus on the comparison of X-ray and optical observations, previously investigated only separately by Ricci et al. (2018) and Balmaverde et al. (2021), respectively.

This manuscript is organized as follows. A brief description of 3CR 196.1 is given in Section 2. Astrometric registration of all images is reported in Section 3, together with details about data reduction procedures for optical and X-ray data sets. The results and discussion on them are presented in Section 4 and Section 5, respectively, while Section 6 is devoted to our conclusions.

We adopted cgs units for the numerical results and assumed a flat cosmology with H_0=69.6 km s^{-1} Mpc^{-1}, $\Omega_M = 0.286$, and $\Omega_\Lambda = 0.714$ (Bennett et al. 2014), unless otherwise stated. At the source redshift (i.e., z=0.198) the physical scale is 3.299 kpc arcsec^{-1}. Standard astronomical orientation (north upward and east to the left) is adopted throughout the paper.

2. The Strange Case of 3CR 196.1

3CR 196.1 is the radio galaxy associated with the brightest cluster galaxy of the galaxy cluster CIZA J0815.4-0303 (Kocevski et al. 2007). From an optical perspective, this radio galaxy is classified as a low-excitation radio galaxy (Buttiglione et al. 2010), while at radio frequencies it presents a hymor radio structure (see Gopal-Krishna 2000), with a classical edge-darkened morphology, typical of FR Is, toward the southwest and a radio lobe, typical of FR IIs on the opposite side (Fanaroff & Riley 1974).

Near-infrared (Madrid et al. 2006) and optical continuum observations (Baum et al. 1988; de Koff et al. 1996) revealed that the host galaxy of 3CR 196.1 shows an elliptical morphology elongated from northeast to southwest, in the same direction as the radio jet. Optical images also revealed the presence of periodic shells possibly due to past merger events (Zirbel 1996), in agreement with centroid shifts measured using optical isophotes of its host galaxy (de Koff et al. 1996). Additionally, using HST emission line images, Baldi et al. (2019) measured a lower limit for the total ionized gas mass for 3CR 196.1 of $3.5{\cdot}10^5$ $M_\odot$, using the nuclear electron density. The analysis of newly obtained MUSE data focused on the [O III]λ5007 properties by Speranza et al. (2021) revealed a broad blue [O III]λ5007 component with a maximum velocity of ∼-640 km s^{-1}, extending toward the northeast, in the same direction as the radio jet.

Ricci et al. (2018) confirmed the presence of an X-ray surface brightness depression, previously suggested by Massaro et al. (2012), by carrying out a multiwavelength analysis of archival radio, optical, and X-ray observations. This surface brightness depression indicates the presence of a "butterfly-shaped" cavity at ∼10 kpc from the nucleus (see left panel of Figure 1). The temperature of the galaxy cluster (∼4.2 keV) drops to ∼2.8 keV in the inner 30 kpc, suggesting that 3CR 196.1 is the brightest cluster galaxy of a cool-core cluster.

At scales of tens of kpc, the Hα + [N II]λ6584 emission observed with the HST is spatially aligned with the radio jet and lies in the base of the X-ray cavity. Lastly, Ricci et al. (2018) concluded that 3CR 196.1 could be an example where cold gas is being uplifted by radio lobes and that it could have undergone several AGN outbursts at multiple epochs. They also suggested that its galaxy cluster may have experienced a merger episode, as revealed by the spiral pattern seen in the X-ray observation, characteristic of gas sloshing (see, e.g., Markevitch & Vikhlinin 2007).

3. Data Analysis Procedures

The X-ray data employed for this work are ∼8 ks archival Chandra observations (ObsID 12729). The MUSE data set was obtained from the MURALES survey (ID 0102.B-0048(A); two 10 minute exposures). Details on these observations as well as on the Chandra and MUSE data reduction and analyses can be found in Ricci et al. (2018) and Balmaverde et al. (2021), respectively.

3.1. Astrometric Registration

Astrometric registration was carried out by comparing 8.4 GHz Very Large Array (VLA[19]), Panoramic Survey Telescope and Rapid Response System (Pan-STARRS)[20] r-band, MUSE, and Chandra images. An image showing the sources used for the registration can be found in Appendix A.

We decided against registering the Chandra image as the nucleus of 3CR 196.1 is not detected in the Chandra image, and the typical shift applied to Chandra images is <0.″7 (Massaro et al. 2011), which corresponds to a shift of less than 2 pixels in our X-ray images and thus is sufficiently accurate for our comparison. Additionally, no registration was performed on the radio as the radio core is not detected in the available radio maps and their positional uncertainty is <0.″03 (adopting a conservative VLA uncertainty of 10% of the beam size[21]). Thus, the final astrometric registration of MUSE data relied on the Pan-STARRS r-band image as all sources in the MUSE data were also detected in Pan-STARRS. A detailed description of the strategy adopted to register the data can be found in Appendix A.

3.2. Chandra Data Analysis

We performed the X-ray data reduction following the standard procedures of the Chandra Interactive Analysis of

[19] https://science.nrao.edu/facilities/vla/archive/index
[20] https://catalogs.mast.stsci.edu/panstarrs/
[21] https://science.nrao.edu/facilities/vla/docs/manuals/oss/performance/positional-accuracy

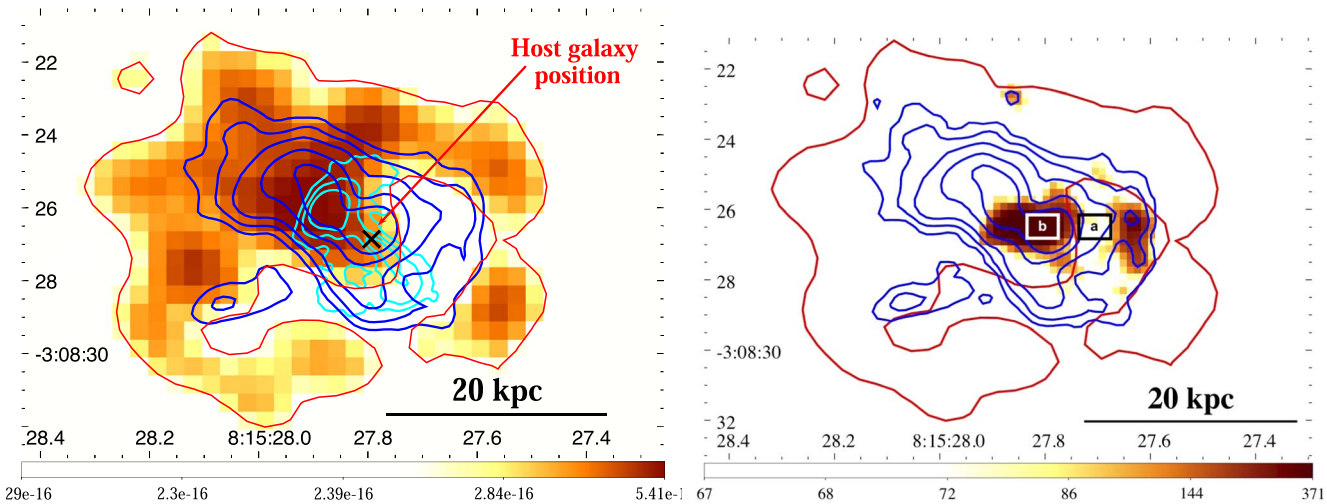

Figure 1. Left: Exposure-corrected 0.7–2 keV Chandra image of 3CR 196.1 with Hα + [N II]λ6584 (blue) and 8.4 GHz VLA (cyan) contours. The position of the centroid of the optical host, which corresponds to the radio core position is shown as a black cross. The Chandra image has a pixel scale of 0.″492 (corresponding to ~1.6 kpc) and was smoothed with a 1.″5 radius Gaussian kernel. X-ray contours are drawn at 0.25 $\cdot$ 10^{-15} erg cm^{-2}s^{-1}. Hα + [N II]λ6584 contours were drawn at 5, 10, 20, 50, and 100 times the rms. 8.4 GHz VLA contours were drawn at 5, 20, and 50 times the rms level of the background. Hα and the [N II]λ6584 emission present an offset with respect to the borders of the X-ray cavity. The northeastern radio lobe is co-spatial with the X-ray emission peak, while the southwestern lobe is co-spatial with the X-ray cavity. Right: Redward [N II]λ6584 emission with the same exposure-corrected 0.7–2 keV Chandra contours (red) and Hα + [N II]λ6584 contours (blue) overlaid as in the left panel. The (a) and (b) regions marked in the figure show the extraction areas of the spectra in Figure 2.

Observations (CIAO; Fruscione et al. 2006) v4.11 threads,[22] adopting the Chandra Calibration Database v4.8.4.1 (for an in-depth analysis of the X-ray observation see Ricci et al. 2018).

X-ray flux maps were created by taking the exposure time and the effective area into account. X-ray maps presented in this work were restricted to 0.7–2 keV to highlight the soft diffuse X-ray emission by using monochromatic exposure maps set to the nominal energies of 1.2 keV. The flux map was converted from units of counts s^{-1} cm^{-2} to cgs units by multiplying each event by the nominal energy of the band, assuming that every event in the same band has the same energy (see Massaro et al. 2015).

3.3. MUSE Data Analysis

Regarding the MUSE data analysis, we obtained the fully reduced data cube from the ESO archive.[23] We measured the redshift by using the Penalized Pixel-Fitting code (Cappellari 2017) to fit the stellar continuum and absorption features in a 2″ radius circular region centered on the host position. Following this procedure, we measured a value for the redshift of $z = 0.1982$, which we adopted throughout our analysis.

3.3.1. Large-scale Ionized Gas

We subtracted the continuum spaxel by spaxel from the archival MUSE reduced data in two different ranges: blue range from 5370 to 6170 Å and red range from 7170 to 8680 Å, by fitting the continuum in each range using a power law. We fitted the Hβ and [O III]$\lambda\lambda$4960, 5008 lines in the continuum-subtracted blue range and the [O I]λ6300, Hα, [N II]$\lambda\lambda$6548, 6584, and [S II]$\lambda\lambda$6718, 6733 lines in the continuum-subtracted red range. In general, we fitted each line with a single Gaussian component, fixing the wavelength separation between lines as well as the line ratio of the [N II]$\lambda\lambda$6548, 6584 and [O III] $\lambda\lambda$4960, 5008 components, to their theoretical value of 1/3 (adopting CASE B; see Osterbrock & Ferland 2006).

3.3.2. Central Region

Although a single Gaussian was adequate to fit the spectral components in most spaxels, we found that the spectra in the central area and the X-ray cavity region have additional components in Hα, [N II]λ6584 and [S II]$\lambda\lambda$6718, 6733. The position of the redward [N II]λ6584 emission is shown in the right panel of Figure 1.

To illustrate these redward components, we chose two regions in the central area of 3CR 196.1, regions *a* and *b*, shown in the right panel of Figure 1. Both these regions were chosen to be close to the central region, so that the signal-to-noise was the highest and with sizes large enough to match the seeing (i.e., 1″), but not so large that the kinematics of the ionized gas would compromise the identification of the different spectral components. Additionally, region *a* was chosen to contain only a single spectral feature for each emission line, while region *b* was chosen to illustrate a region with both "rest-frame" and redward components.

A comparison of the spectra extracted from regions *a* and *b* is shown in Figure 2, where the rest-frame wavelengths of lines are marked in black and those of the redward components are marked in red. Although there appear to be possible additional spectral features corresponding to the Hβ and [O I]λ6300 lines, these components are not detected (with a significance below 2σ). The spectral position of the reward components in region *b* in Figure 2 corresponds to ~21 Å (i.e., ~1000 km s^{-1}) from the rest frame and was derived on the basis of the spectral fit performed on the spectrum extracted from region *b*. This fit, shown in Figure 3, was performed using two Hα + [N II]λ6584 triplets, one at the rest frame and one redshifted by ~21 Å, and it shows how the spectrum from region *b* cannot be reproduced without introducing an additional redward component.

These redshifted spectral features are spectrally blended with emission at the systemic redshift, i.e., the redward and

[22] http://cxc.harvard.edu/ciao/threads/
[23] http://archive.eso.org/scienceportal/home

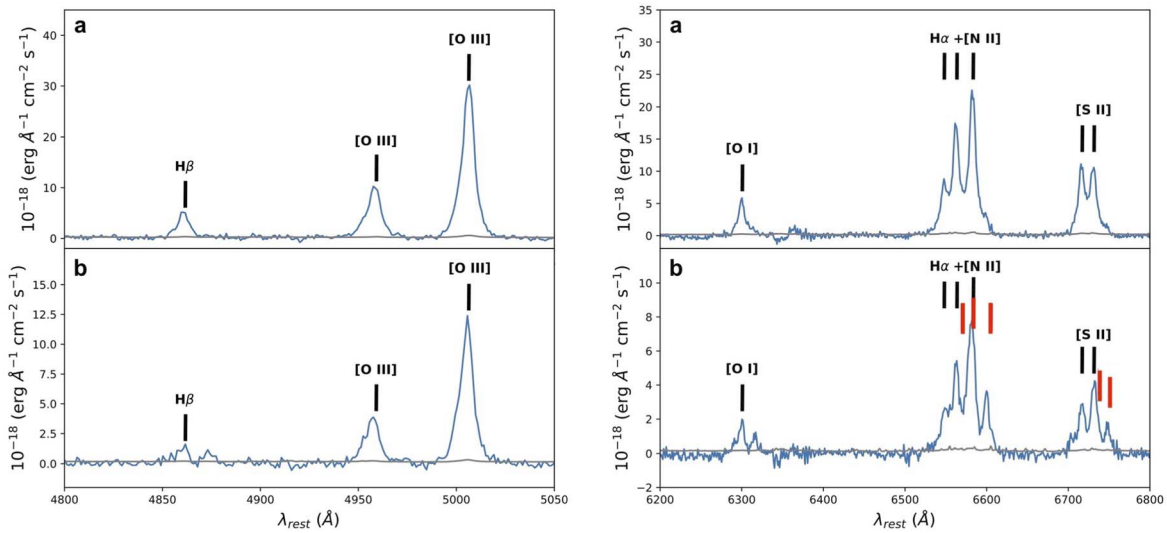

Figure 2. Spectra extracted from regions *a* and *b* (top and bottom panels in Figure 1, right panel, respectively). The top spectrum could be fitted using a single Gaussian component for each line, while the bottom one shows an extra redward component in all lines except for the Hβ and [O III]$\lambda\lambda$4960, 5008 lines. Black markers point to the rest-frame position of each line while red markers are located at 21 Å from the rest frame ($\sim$1000 km s^{-1}). The uncertainties in the spectra are shown in gray.

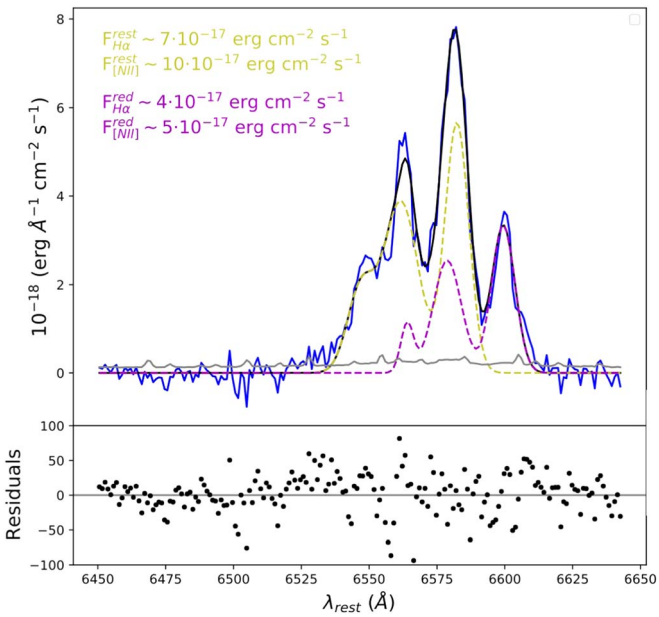

Figure 3. Fit to the spectrum extracted from region *b* (i.e., a 1 arcsec^2 region, as shown in the right panel of Figure 1) using one Hα + [N II]λ6584 at the rest frame (yellow) and another one redshifted by $\sim$21 Å. The uncertainties in the spectrum are shown in gray. The spectra in region *b* (see right panel of Figure 1) cannot be reproduced using a single triplet.

"rest-frame" components have an offset consistent with the separation between the Hα and the [N II]λ6584 lines (see Figure 2). This offset, together with the fact that this redward component overlaps, in projection, with the AGN emission as well as with the low signal-to-noise of the [N II]λ6548 line, introduces a degeneracy in the intensities of the Hα, [N II] $\lambda\lambda$6548, 6584, and [S II]$\lambda\lambda$6718, 6733 lines that we cannot break without knowing a priori the ionization status of the source and the density of the gas. Thus, the limited spectral ($\sim$50 km s^{-1}) and spatial ($\sim$1″) resolutions of MUSE cubes prevent us from breaking the degeneracy, and from providing a thorough analysis of the kinematics and ionization state of the gas.

4. Results

We detected Hα+[N II]λ6584 emission spatially associated with the X-ray cavity (see left panel of Figure 1) and, at the same time, did not detect Hβ or [O III]λ5007 emission in the X-ray cavity region (see left panel of Figure 4). A comparison between X-ray and Hα+[N II]λ6584, [O III]$\lambda\lambda$4960, 5008, and [S II]$\lambda\lambda$6718, 6733 is shown in the left panel of Figure 1 and the left and right panels of Figure 4, respectively. Additionally, the flux, velocity, and velocity dispersion maps for all emission lines in the MUSE observed range are shown in Figure 8 in Appendix B.

The morphology of the Hα+[N II]λ6584 hints at differences in the density of the environment. In particular, the northeastern component (region L in the left panel of Figure 4) being co-spatial with the northeastern radio lobe and with the highest X-ray surface brightness peak indicates a denser environment toward the northeast than toward the southwest, where the X-ray cavity is located.

We decided to give an overview of the gas kinematics via velocity channel maps, as shown in Figure 6, as the blending of the spectral components (see Figure 3) and the low signal-to-noise ratio in the cavity region prevent us from drawing strong quantitative conclusions from the study of the kinematics of each component. This approach is commonly used for isolated lines. Thus, to avoid contamination due to emission lines being part of a triplet, we considered different reference lines for blue and redshifted emission. We considered as blueshifted, emission blueward of the [N II]λ6548 rest-frame line and, as redshifted, emission redward of the [N II]λ6584 rest frame. Therefore, the central wavelength range including the emission of the Hα+[N II]λ6584, dominated by spectral blending, is not shown in the channel maps. Channel maps are shown in increments of 100 km s^{-1}, which correspond to two resolution elements, with the exception of the central channels that are shown in increments of 50 km s^{-1}.

The velocity channel maps show that the blueshifted emission is co-spatial with the northeastern radio lobe (region L). Additionally, there seems to be a filament of blueshifted emission on the outer edge of the southern radio lobe (F1). The

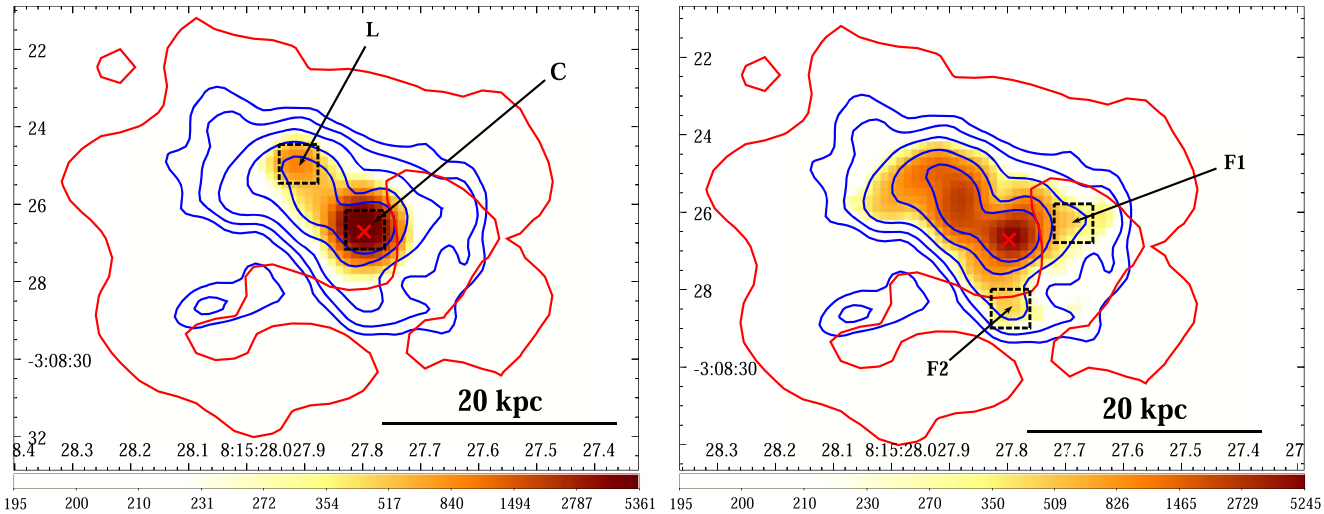

Figure 4. [O III]$\lambda\lambda$4960, 5008 (left) and [S II]$\lambda\lambda$6718, 6733 (right) emission with the exposure-corrected 0.7–2 keV Chandra contours (red) and Hα + [N II]λ6584 contours (blue) overlaid. The position of the centroid of the optical host is indicated with a red cross. The 1 arcsec^2 extraction regions, L, C, F1, and F2, for the BPT diagram in Figure 5 are shown as black dashed squares. Chandra contours were smoothed with a 1.5″ Gaussian kernel radius and drawn in red at $0.25 \cdot 10^{-15}$ erg cm^{-2} s^{-1}. Hα + [N II]λ6584 contours were drawn at 5, 10, 20, 50, and 100 times the rms. Region L marks the region co-spatial with the northeastern radio lobe.

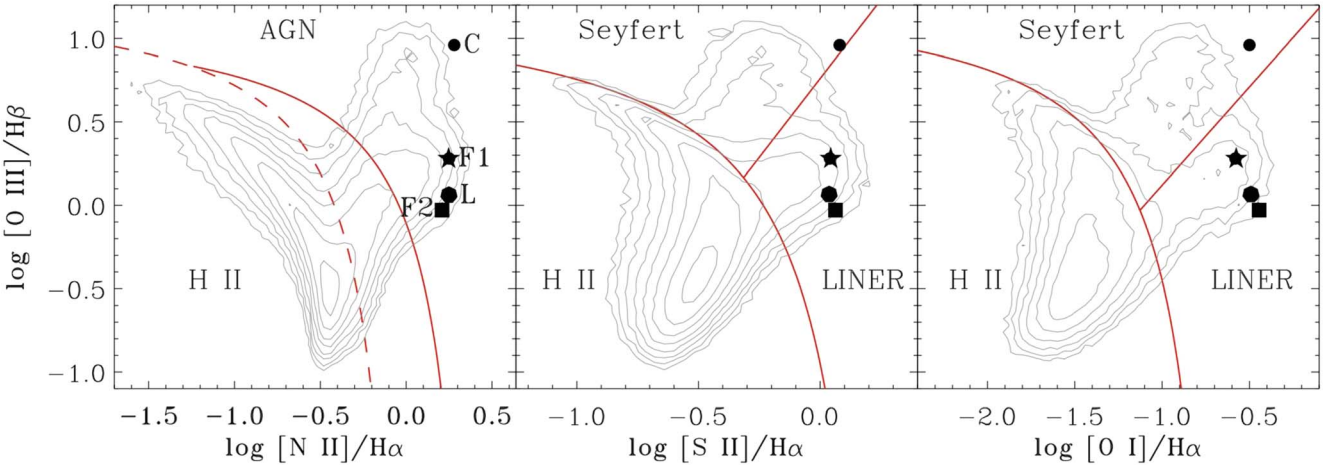

Figure 5. Location of 3CR 196.1 regions core, northeastern radio lobe and blue and red filaments (C, L, F1 and F2, respectively) in the BPT diagnostic diagrams. The size of the regions was chosen to match the seeing of MUSE observations (i.e., ∼1″). The extraction regions are shown in Figure 4. The red solid curves represent the Kewley et al. (2001) theoretical upper bound for pure star formation, the red straight line shows the Kewley et al. (2006) separation between AGN and LINERs, while the dashed red curve in the [N II]λ6584 BPT is the Kauffmann et al. (2003) empirical classification separating star-forming galaxies and AGN. Contours represent the isodensities of all Sloan Digital Sky Survey Data Release 7 emission line galaxies (Capetti & Baldi 2011). Extended ionized gas structures in 3CR 196.1 have an ionization state compatible with the LINER region of the BPT diagnostic diagrams, while the ionization state at the optical host position is compatible with Seyfert-like ionization.

redshifted emission, up to ∼300 km s^{-1}, shows some extended emission that appears to follow the northeastern radio jet and a filament that seems to wrap around the southern lobe (F2). There also appears to be some emission connecting filaments F1 and F2, which is most visible at ∼400 km s^{-1} (A). This arched feature is apparently tracing the inner edge of the X-ray cavity. Lastly, at the reddest velocities (>500 km s^{-1}), the only emission that is detected corresponds to the redward [N II] λ6584 shown in the right panel of Figure 1 and in the spectrum of region *b* in Figure 2 (region R).

All extended ionized gas features, i.e., the lobe and red and blueshifted filaments (regions L, F1 and F2, marked in Figure 4) present LINER-like ionization states, as shown in the Baldwin–Phillips–Terlevich (BPT) diagram in Figure 5 (see, e.g., Baldwin et al. 1981 and Kewley et al. 2006). The only region shown in Figure 5 with a Seyfert-like ionization state is the region corresponding to the optical host position. The position in the BPT diagram of the extra redward component shown in Figure 1, right panel, could not be established as the spectral and spatial blending does not allow us to obtain estimates of the line ratios in this region with the current signal-to-noise ratio of our MUSE data. All extraction regions used for the BPT diagram were selected on the basis of specific morphology/kinematics of the source and are shown in Figure 4. Additionally, all regions have a size of ∼1 arcsec^2, to match the seeing of the observation.

5. Discussion

Multiphase gas halos, surrounding AGN hosted in Brightest Cluster Galaxies (BCGs) harbored in cool-core galaxy clusters, represent one of the keys to understanding AGN feedback

mechanisms. Currently, the main hypothesis for the origin of ionized gas in these halos is the cooling and condensation of the hot, X-ray emitting plasma, often in the shape of (i) filaments (see, e.g., Fabian et al. 2008, 2011; Fabian 2012; Gaspari et al. 2017, 2018; Qiu et al. 2020; Jimenez-Gallardo et al. 2021; Qiu et al. 2021), (ii) rotating disks (see, e.g., Wilman et al. 2005; Hamer et al. 2014), or (iii) plumes (see, e.g., Hamer et al. 2012, 2016; Pasini et al. 2019). One of the most remarkable examples of ionized gas filaments in a cool-core cluster can be found in NGC 1275 in the center of the Perseus galaxy cluster (Lynds 1970; Conselice et al. 2001 and Fabian et al. 2008), where ionized gas filaments are spatially associated with an X-ray excess (Fabian et al. 2011). The same situation occurs for other BCGs of cool-core clusters, where a tight connection between X-ray and optical filamentary emission was found, such as the cases of A1795 (Crawford et al. 2005), A1644 (McDonald et al. 2010), A2597 (Tremblay et al. 2016), and MKW 3 s (Jimenez-Gallardo et al. 2021).

Ionized gas filaments have also been found surrounding X-ray cavities, i.e., co-spatial with the rims of X-ray cavities (see, e.g., works on A2052 by Blanton et al. 2011 and Balmaverde et al. 2018, as well as works by Lim et al. 2008, Tremblay et al. 2015, and Olivares et al. 2019). However, ionized gas spatially associated, and thus, potentially filling an X-ray cavity, is a rare occurrence with no clear explanation. In this work, we present the potential first detection of ionized gas spatially associated with an X-ray cavity, using Hα + [N II]λ6584 emission as a tracer. Although the scenario were this ionized gas is actually overlaid to the X-ray cavity cannot be conclusively excluded, it appears unlikely. If that was the case, we would expect to see ionized gas spatially associated with the outer borders of the X-ray cavity, where its column density would be the highest, instead of with the X-ray cavity.

5.1. The Northeastern Plume

Similar to other cool-core galaxy clusters such as A1991, A3444, Ophiuchus (Hamer et al. 2012), A111, A133, A2415 (Hamer et al. 2016), and A2495 (Pasini et al. 2019), the peak of the X-ray emission surrounding 3CR 196.1 does not correspond to the position of the BCG, presenting an offset of $\sim$2″ (i.e., $\sim$6.5 kpc; see left panel of Figure 2). Such offsets have been interpreted as caused by sloshing of the ICM due to events such as minor mergers. Typically, in those cases, the ionized gas forms plumes either following the X-ray peak or connecting the X-ray peak and the BCG. However, in the case of 3CR 196.1, we argue that the X-ray peak seen in the ICM is most likely caused by the interaction of the northeastern radio jet with the ICM, as seen in 3CR 171 and 3CR 305 (Hardcastle et al. 2010, 2012), due to the alignment between the northeastern radio lobe and the X-ray peak, as well as to the "hammerhead" shape of the northeastern radio lobe and the ionized gas plume extending in the direction opposite to the position of the BCG (see Figure 4). Thus, the ionized gas corresponding to region L could originate from the cooling of the jet-heated ICM. This origin is compatible with the ionized gas presenting a LINER-like ionization state, as shown in Figure 5 as LINER-like emission in extranuclear regions is often associated with large-scale outflows and shocks or with radio jet-shocked regions (see Kewley et al. 2006 and references therein).

5.2. Ionized Gas Filaments around 3CR 196.1

One of the most likely mechanisms responsible for the formation of ionized gas filaments in cool-core galaxy clusters is chaotic cold accretion (CCA; see Gaspari et al. 2012; Gaspari & Ruszkowski 2013; Gaspari et al. 2015, 2017, 2018), i.e., the condensation of the hot plasma in the ICM and its precipitation onto the black hole. ICM cooling due to nonlinear thermal instabilities was first introduced by Pizzolato & Soker (2005) as "cold feedback". More recently, Gaspari et al. (2018) adopted the ratio of the cooling time and the eddy turnover time, $C = t_{\rm cool}/t_{\rm eddy}$, as a tool to assess the multiphase state of a system, with $0.6 < C < 1.8$ marking the extent of the condensation region. We applied this criterion to 3CR 196.1, where we assumed $t_{\rm cool} \sim 500$ Myr, as obtained by Ricci et al. (2018) for the inner region (i.e., 10″ or $\sim$30 kpc radius), as currently available X-ray observations did not allow us to carry out a more detailed spectral analysis. We obtained the eddy turnover time, as a function of the distance to the galaxy cluster core, as $t_{\rm eddy} = 2\pi \frac{r^{2/3}L^{1/3}}{\sigma_{v,L}}$ (see Gaspari et al. 2018), where $L \sim 10$ kpc is the injection scale, traced by the diameter of the X-ray cavity, and $\sigma_{v,L} \sim 212$ km s^{-1} is the velocity dispersion at the injection scale. Thus, significant precipitation is expected to occur within a region of $r \sim$ 9-48 kpc radius, where $C \approx 1$. As the blue and red filaments at the edges of the southern radio lobe (F1 and F2 in the right panel of Figure 4) extend up to 10 kpc (where $C \sim 1.7$), and the small ionized gas filament, F3, extends up to 15 kpc (where $C \sim 1.3$) to the southeast (see Figure 6), the origin of ionized gas filaments surrounding 3CR 196.1 is compatible with a condensation rain. Moreover, the velocity and velocity dispersion along filament F2, $\sim$200 km s^{-1} and $\sim$100 km s^{-1}, respectively, are consistent with those literature observations compared with CCA simulations by Gaspari et al. (2018). Therefore, 3CR 196.1 presents possible signs of black hole feeding.

Alternatively, as proposed, for instance, in simulations by Qiu et al. (2020, 2021), ionized gas filaments in 3CR 196.1 could be due to AGN outflows uplifting warm ($10^4 < T \leqslant 10^7$ K) gas from the central 2 kpc of the galaxy cluster, which then experiences radiative cooling. The energy needed to inflate adiabatically an ionized gas bubble with a radius $r \sim 5$ kpc, i.e., the size of the arched structure A in Figure 6, and velocity $v \sim 400$ km s^{-1}, in an ambient medium with density $n_0 = 0.098$ cm^{-3}, as obtained by Ricci et al. (2018) for the inner $\sim$30 kpc of 3CR 196.1, can be obtained following the approach described by Nesvadba et al. (2006):

$$\dot{E} \approx 1.5 \cdot 10^{46}\, r_{10}^2\, v_{1000}^3\, n_0 \text{ erg s}^{-1}, \quad (1)$$

where r_{10} is the radius of the bubble in units of 10 kpc, and v_{1000} is the velocity in units of 1000 km s^{-1}. Thus, the minimum energy needed to inflate such a bubble, $\dot{E} \sim 2.4 \cdot 10^{43}$ erg s^{-1}, is an order of magnitude below the jet power obtained by Ricci et al. (2018), $P_{\rm jet} \sim 1.9 \cdot 10^{44}$ erg s^{-1}, and therefore the ionized gas spatially associated with the X-ray cavity is consistent with a bubble being inflated by the radio jet.

The electron density in filaments F1 and F2 can be estimated using the [S II]$\lambda\lambda$6718, 6733 duplet ratio as described in Sanders et al. (2016). We selected two regions of the size of the point-spread function (PSF) ($\sim$1.″0) over the filaments to compute the electron density. Thus, the electron density within the cavity is <350 e$^-$ cm^{-3}. This density is comparable with

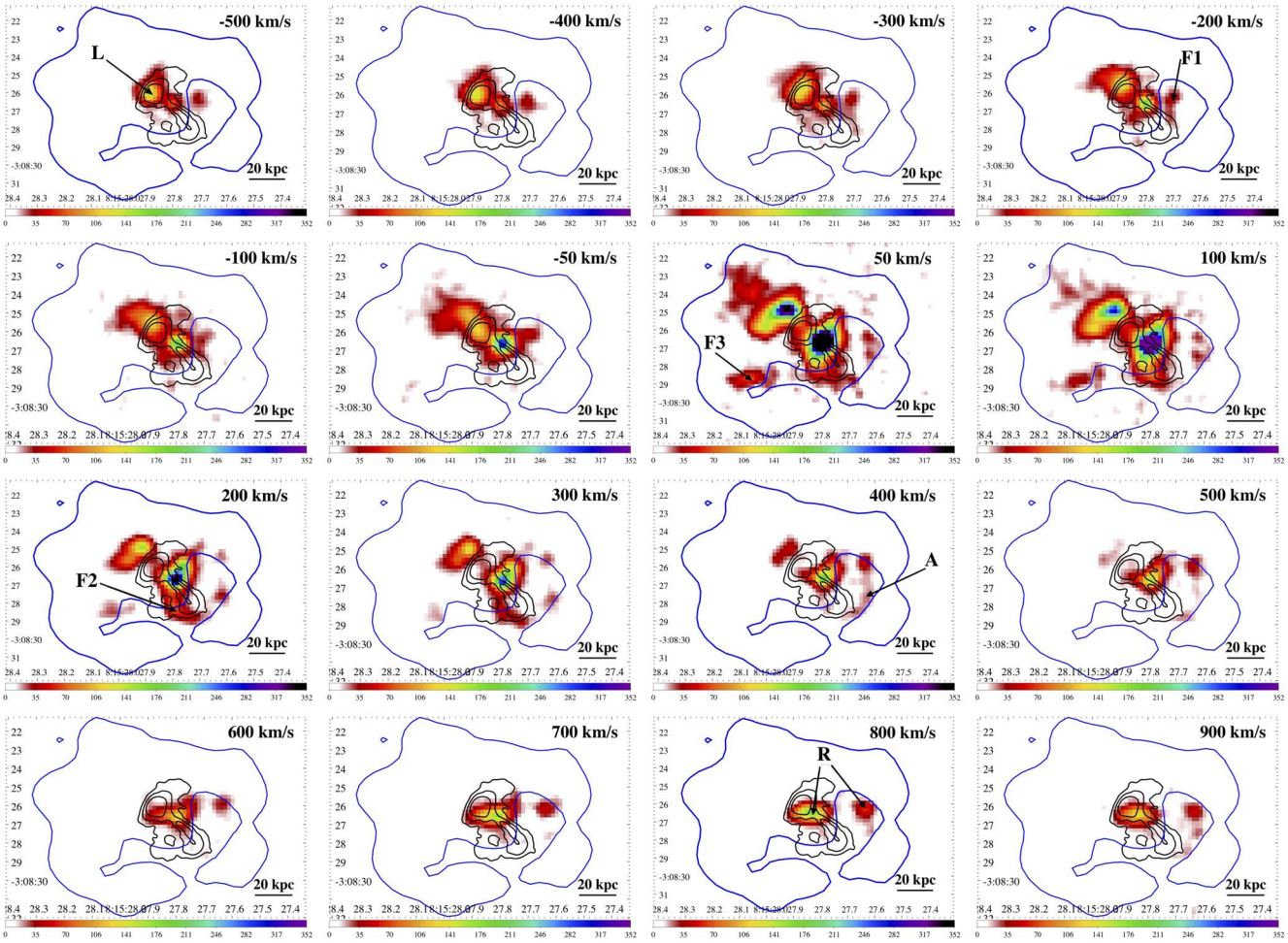

Figure 6. Hα + [N II]λ6584 flux in velocity bins of 100 km s^{-1}, with 8.4 GHz VLA (black) and exposure-corrected 0.7–2 keV Chandra (blue) contours overlaid. MUSE images have a pixel size of 0.″2 pixel^{-1}. 8.4 GHz VLA contours were drawn at 5, 20, and 50 times the rms level of the background. Chandra contours were smoothed with a 1.″5 Gaussian kernel radius and drawn in red at $0.25 \cdot 10^{-15}$ erg cm^{-2} s^{-1}. The centers of the velocity bins are shown on the top right corners. The main features are labeled in the figures, with L denoting the region co-spatial with the northeastern radio lobe, F1 and F2 denoting the blue and red filaments that appear to surround the southwestern radio lobe, A being the arched emission that appears to trace the inner edge of the X-ray cavity, F3 marking an additional filament not co-spatial with the X-ray cavity, and R being the region polluted by the redward component.

that of the filaments found surrounding an X-ray cavity in A2052 by Balmaverde et al. (2018), which were interpreted as being caused by an expanding bubble, as well as with other filaments in cool-core galaxy clusters (see, e.g., McDonald et al. 2012; Jimenez-Gallardo et al. 2021). Additionally, extended ionized gas features, corresponding to filaments F1 and F2, could be interpreted as being caused by the interaction of the southern radio jet with its surrounding medium, as the filaments present LINER-like ionization states, as shown in Figure 5.

Lastly, similarly to the expanding bubble in A2052, filaments F1 and F2 in 3CR 196.1 are blueshifted and redshifted, respectively, and a potential region with split lines that could be due to the overlap of the emission of both filaments, a typical sign of an expanding bubble (Balmaverde et al. 2018), is also found to be co-spatial with the X-ray cavity (region R in Figure 6). If that is the case, the expansion velocity of the bubble, which can only be estimated indirectly through X-ray observations, could be measured as the maximum velocity observed at the arched structure, A, i.e., ∼400–500 km s^{-1}. Nevertheless, due to the low signal-to-noise ratio in the cavity region of current MUSE observations, the kinematics of the ionized gas filaments cannot be firmly derived, and thus this scenario cannot be confirmed.

5.3. The Central Region of 3CR 196.1

During this analysis, we discovered that, in the central and X-ray cavity regions, all spectral features, except for the Hβ, [O III]$\lambda\lambda$4960, 5008, and [O I]λ6300 lines, have an additional component at ∼1000 km s^{-1} toward the red of the rest frame (see right panel of Figure 1 and Figures 2 and 3). This additional redward component could be due to a background gas cloud as there does not appear to be a continuous range of velocities from the rest frame to the redward component that would indicate the presence of an outflow. This emission could also be due to filaments of ionized gas being accreted onto the black hole through CCA, similarly to filament F3. Despite that, the spatial resolution (∼1″) of the current observations together with the blending of lines in the Hα + [N II]λ6584 complex due to the limited spectral resolution (∼50 km s^{-1}) prevent an in-depth analysis on the kinematics and ionization state of the gas in the central and X-ray cavity regions with current signal-to-noise ratios.

6. Summary and Conclusions

We carried out a comparison of optical VLT/MUSE and X-ray Chandra observations of 3CR 196.1, the central radio galaxy associated with the cool-core galaxy cluster CIZAJ0815.4-0303, which exhibits a "butterfly-shaped" X-ray cavity at $\sim$10 kpc toward the southwest of the nucleus. Through this analysis, we detected the presence of ionized gas spatially associated with an X-ray cavity.

The main possible explanations for detecting Hα + [N II] λ6584 emission spatially associated with an X-ray cavity instead of with its rim include:

1. The ionized gas is actually concentrated in filaments that wrap around the X-ray cavity, such as the ones shown in Figure 6. However, due to projection effects, as well as to the presence of an additional redward component in the cavity region (see right panels of Figures 1 and 2), the ionized gas appears to be co-spatial with the X-ray cavity. We tend to disfavor this scenario as it implies that we would be seeing the gas where it has the lowest column density along the line of sight, instead of at the edges, where its column density would be the highest.
2. The ionized gas is actually filling the X-ray cavity. In that case there could be two possible explanations: (i) the gas has undergone multiple ionization events due to different AGN outbursts, or (ii) the ionized gas is forming filaments originating from the cooling of warm ($10^4 < T \leqslant 10^7$ K) AGN outflows. Scenario (i) is compatible with an AGN outburst occurring after the one responsible for the X-ray cavity, as the typical cycling times between quiescence and activity in radio galaxies are $\sim 10^7$–10^8 yr (see Shabala et al. 2008 and references therein), and the estimated age of the X-ray cavity is 12 Myr (Ricci et al. 2018). On the other hand, scenario (ii) is compatible with simulations by Qiu et al. (2020), which show that warm ($10^4 < T \leqslant 10^7$ K) gas present in the central 2 kpc of galaxy clusters (due to radiative feedback) could be lifted by AGN outflows and radiatively cooled, forming ionized gas filaments. Additional simulations in Qiu et al. (2021) showed that these filaments could be shaped as rings perpendicular to the direction of the outflow, which would explain the arched feature (A in Figure 6), that appears to connect filaments F1 and F2 (surrounding the southwestern radio lobe in Figure 4, right panel) and that seems to trace the inner edge of the X-ray cavity.

To distinguish between these scenarios, additional observations would allow us to characterize, in more detail, the temperature and density profiles of the central ICM emission. To characterize the ionized gas, we would also need deeper and higher spatial resolution MUSE observations with, e.g., the adaptive optic-assisted MUSE narrow-field mode. Alternatively, the new Enhanced Resolution Imager and Spectrograph at the VLT, or the NIRSPEC Integral Field Unit on the James Webb Space Telescope, could help us understand the origin of the additional redward component found in the spectra, as well as to derive the kinematics of the ionized gas spatially associated with the X-ray cavity. Such observations would allow us to measure the expansion velocity in the case in which the ionized gas is tracing an expanding bubble.

We thank the anonymous referee for their useful comments that led to the substantial improvement of the paper. A.J. thanks M. Gaspari for his feedback on Chaotic Cold Accretion. F.M. is in debt to S. Bianchi for his valuable input on X-ray photoionization scenarios. This work is supported by the "Departments of Excellence 2018-2022" Grant awarded by the Italian Ministry of Education, University and Research (MIUR) (L. 232/2016). This research has made use of resources provided by the Ministry of Education, Universities and Research for the grant MASF_F-FABR_17_01. This investigation is supported by the National Aeronautics and Space Administration (NASA) grants GO9-20083X and GO0-21110X. A.J. acknowledges the financial support (MASF_CONTR_FIN_18_01) from the Italian National Institute of Astrophysics under the agreement with the Instituto de Astrofisica de Canarias for the "Becas Internacionales para Licenciados y/o Graduados Convocatoria de 2017". F.R. acknowledges support from PRIN MIUR 2017 project "black hole winds and the Baryon Life Cycle of Galaxies: the stone-guest at the galaxy evolution supper", contract No. 2017PH3WAT. G. V. acknowledges support from ANID program FONDECYT Postdoctorado 3200802. A.P. acknowledges financial support from the Consorzio Interuniversitario per la fisica Spaziale (CIFS) under the agreement related to the grant MASF_CONTR_-FIN_18_02. W.F. and R.K. acknowledge support from the Smithsonian Institution and the Chandra High Resolution Camera Project through NASA contract NAS8-03060. S.B. and C.O. acknowledge support from the Natural Sciences and Engineering Research Council (NSERC) of Canada.

Appendix A
Astrometric Registration

All details related to the strategy adopted to carry out the astrometric registration of MUSE images are reported in the following. We measured the centroids of the optical counterpart of 3CR 196.1 and sources SRC1 to SRC4, in Figure 7, in the Pan-STARRS and MUSE white-light collapsed images and applied the average of the shifts to the MUSE data cube. The final shift was 3.″1 (corresponding to $\sim$10 kpc, which is expected as it is a known issue that MUSE astrometry can be off by several arcseconds, as reported by Prieto et al. (2016),

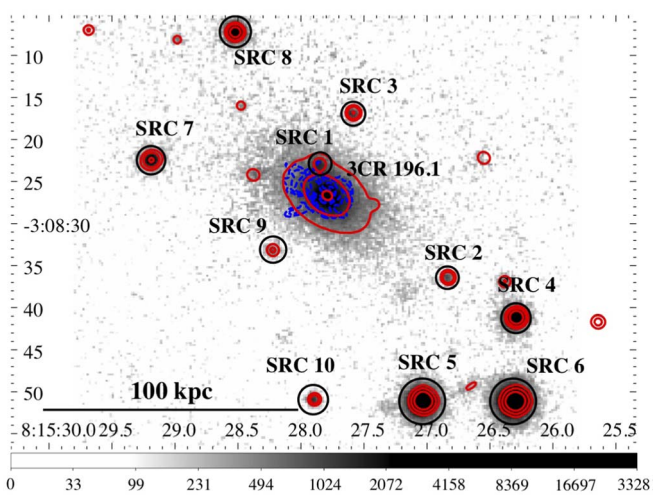

Figure 7. *r*-band Pan-STARRS image with MUSE 4800–6800 Å (red) and MUSE Hα + [N II]λ6584 (blue) contours overlaid. Sources SRC1 to SRC4 were used to compute the shift applied, while sources SRC5 to SRC8 allowed us to verify the registration. MUSE images have a pixel size of 0.″2. 4800–6800 Å contours were drawn at 20, 50, and 200 times the rms level of the background. Hα+[N II]λ6584 contours were drawn at 5, 10, 20, 50, and 100 times the rms level of the background. We found a good alignment between the Pan-STARRS and the MUSE emission applying a shift o 3.″1 (i.e., $\sim$10 kpc).

Balmaverde et al. (2019, 2021), and Tucker et al. (2021)). We then verified that the registration adopted was appropriate for sources SRC5 to SRC8, in Figure 7, by measuring the difference between their centroids in the Pan-STARRS and MUSE white-light collapsed images after the shift. The adopted shift yielded an rms of 0.″18. The final alignment between Pan-STARRS and MUSE data for 3CR 196.1 and the rest of the field sources is shown in Figure 7, for the MUSE white-light image (red contours) and the Hα+[N II]λ6584 emission (blue contours).

Appendix B
Ionized Gas Kinematics

Here we report the flux, velocity, and velocity dispersion maps for the Hβ, [O III]$\lambda\lambda$4960, 5008, [O I]λ6300, Hα, [N II] $\lambda\lambda$6548, 6584, and [S II]$\lambda\lambda$6718, 6733 emission lines (see Figure 8), obtained following the fitting procedure described in Section 3.3, with Chandra and 8.4 GHz contours overlaid in blue and black, respectively. All maps were spatially binned by a factor of 2, resulting on a pixel size of 0.″4 pixel^{-1}, to spatially Nyquist-sample the observation, as the image quality of MUSE data is of the order of 1″. Additionally this binning allows us to better match the resolution of Chandra and to increase the signal-to-noise ratio.

All emission features show similar morphologies and kinematics. The largest blueshift ($\sim$−400 km s^{-1}) can be seen at the termination of the northeastern radio lobe, pointing to the cooling of jet-heated ICM as the origin of ionized gas in the northeast direction. Lastly, the velocity dispersion of all lines is higher ($\sim$200–300 km s^{-1}) in the central $\sim$10 kpc of 3CR 196.1.

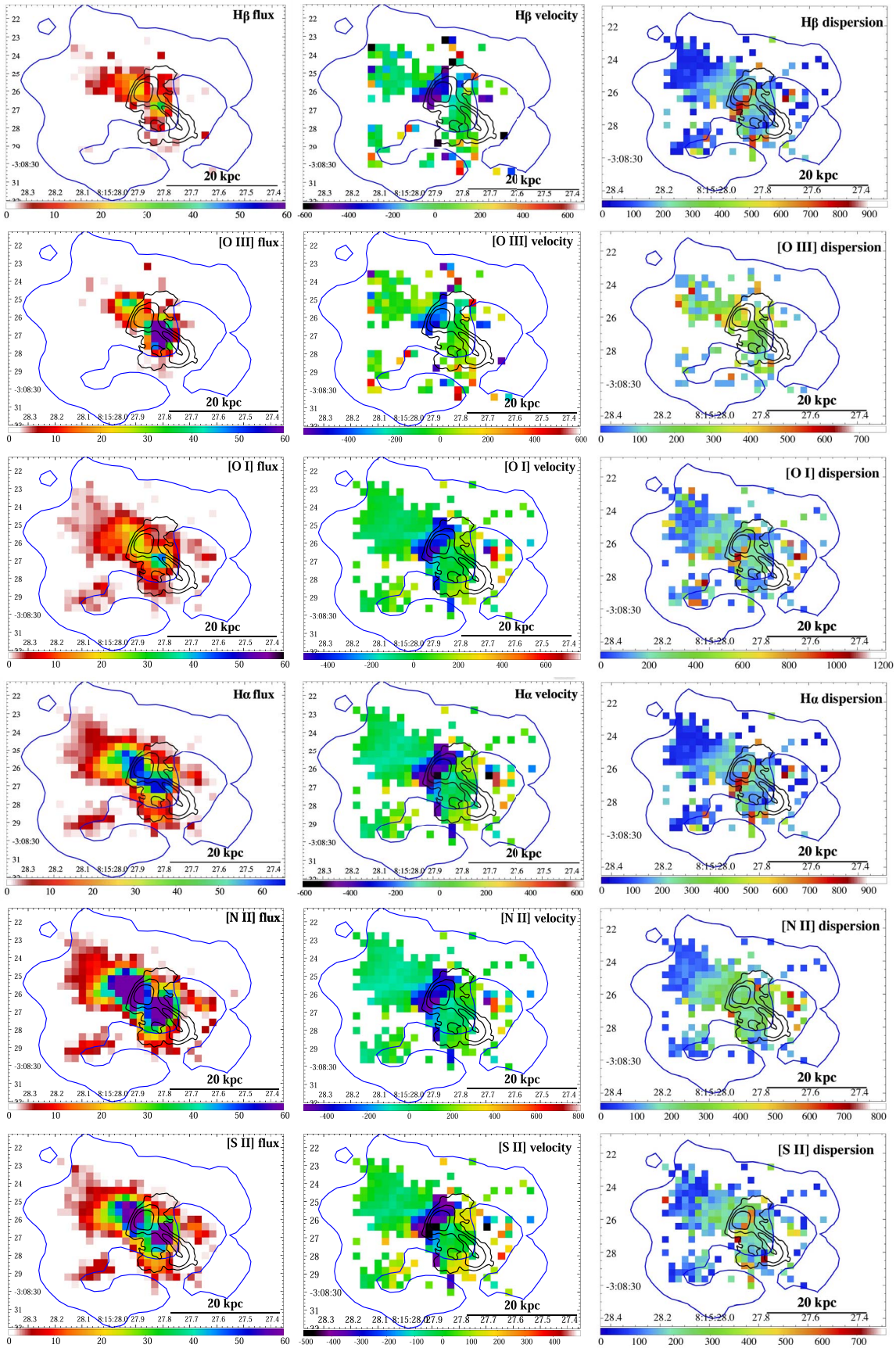

Figure 8. Flux (left), velocity (middle), and velocity dispersion (right) maps with 8.4 GHz VLA (black) and exposure-corrected 0.7-2 keV Chandra (blue) contours overlaid for the Hβ, [O III]$\lambda\lambda$4960, 5008, [O I]λ6300, Hα, [N II]$\lambda\lambda$6548, 6584, and [S II]$\lambda\lambda$6718, 6733 emission lines. MUSE images have a pixel size of 0.4 arcsec/pixel. 8.4 GHz VLA contours were drawn at 5, 20, and 50 times the rms level of the background. Chandra contours were smoothed with a 1.5″ Gaussian kernel radius and drawn in blue at $0.25 \cdot 10^{-15}$ erg cm^{-2} s^{-1}. Flux maps have units of 10^{-17} erg cm^{-2} s^{-1}, while velocity and velocity dispersion maps have units of km s^{-1}.

ORCID iDs

A. Jimenez-Gallardo https://orcid.org/0000-0003-4413-7722
E. Sani https://orcid.org/0000-0002-3140-4070
F. Ricci https://orcid.org/0000-0001-5742-5980
C. Mazzucchelli https://orcid.org/0000-0002-5941-5214
B. Balmaverde https://orcid.org/0000-0002-0690-0638
F. Massaro https://orcid.org/0000-0002-1704-9850
A. Capetti https://orcid.org/0000-0003-3684-4275
W. R. Forman https://orcid.org/0000-0002-9478-1682
R. P. Kraft https://orcid.org/0000-0002-0765-0511
G. Venturi https://orcid.org/0000-0001-8349-3055
M. Gendron-Marsolais https://orcid.org/0000-0002-7326-5793
M. A. Prieto https://orcid.org/0000-0002-3585-2639
A. Marconi https://orcid.org/0000-0002-9889-4238
H. A. Peña-Herazo https://orcid.org/0000-0003-0032-9538
C. P. O'Dea https://orcid.org/0000-0001-6421-054X
L. Lovisari https://orcid.org/0000-0002-3754-2415
R. Gilli https://orcid.org/0000-0001-8121-6177
E. Torresi https://orcid.org/0000-0002-5201-010X
A. Paggi https://orcid.org/0000-0002-5646-2410
V. Missaglia https://orcid.org/0000-0001-8382-3229
G. R. Tremblay https://orcid.org/0000-0002-5445-5401
B. J. Wilkes https://orcid.org/0000-0003-1809-2364

References

Bacon, R., Accardo, M., Adjali, L., et al. 2010, Proc. SPIE, 7735, 773508
Baldi, R. D., Rodríguez Zaurín, J., Chiaberge, M., et al. 2019, ApJ, 870, 53
Baldwin, J. A., Phillips, M. M., & Terlevich, R. 1981, PASP, 93, 5
Balmaverde, B., Capetti, A., Marconi, A., et al. 2018, A&A, 612, A19
Balmaverde, B., Capetti, A., Marconi, A., et al. 2019, A&A, 632, A124
Balmaverde, B., Capetti, A., Marconi, A., et al. 2021, A&A, 645, A12
Baum, S. A., Heckman, T., & van Breugel, W. 1990, ApJS, 74, 389
Baum, S. A., Heckman, T. M., Bridle, A., et al. 1988, ApJS, 68, 643
Bennett, A. S., & Simth, F. G. 1962, MNRAS, 125, 75
Bennett, C. L., Larson, D., Weiland, J. L., & Hinshaw, G. 2014, ApJ, 794, 135
Bîrzan, L., Rafferty, D. A., McNamara, B. R., et al. 2004, ApJ, 607, 800
Blanton, E. L., Randall, S. W., Clarke, T. E., et al. 2011, ApJ, 737, 99
Böhringer, H., Neumann, D. M., Schindler, S., et al. 1996, ApJ, 467, 168
Buttiglione, S., Capetti, A., Celotti, A., et al. 2010, A&A, 509, A6
Capetti, A., & Baldi, R. D. 2011, A&A, 529, A126
Cappellari, M. 2017, MNRAS, 466, 798
Cavagnolo, K. W., McNamara, B. R., Nulsen, P. E. J., et al. 2010, ApJ, 720, 1066
Churazov, E., Forman, W., Jones, C., et al. 2000, A&A, 356, 788
Conselice, C. J., Gallagher, J. S., III, & Wyse, R. F. G. 2001, AJ, 122, 2281
Crawford, C. S., Sanders, J. S., & Fabian, A. C. 2005, MNRAS, 361, 17
de Koff, S., Baum, S. A., Sparks, W. B., et al. 1996, ApJS, 107, 621
Edge, D. O., Shakeshaft, J. R., McAdam, W. B., et al. 1959, MmRAS, 69, 37
Fabian, A. C. 2012, ARA&A, 50, 455
Fabian, A. C., Johnstone, R. M., Sanders, J. S., et al. 2008, Natur, 454, 968
Fabian, A. C., Sanders, J. S., Allen, S. W., et al. 2003, MNRAS, 344, L43
Fabian, A. C., Sanders, J. S., Taylor, G. B., et al. 2006, MNRAS, 366, 417
Fabian, A. C., Sanders, J. S., Williams, R. J. R., et al. 2011, MNRAS, 417, 172
Fanaroff, B. L., & Riley, J. M. 1974, MNRAS, 167, 31P
Forman, W., Churazov, E., Jones, C., et al. 2017, ApJ, 844, 122
Forman, W., Jones, C., Churazov, E., et al. 2005, ApJ, 665, 1057
Fosbury, R. A. E. 1986, in Astrophysics and Space Science Library Vol. 121, Structure and Evolution of Active Galactic Nuclei, ed. G. Giuricin et al. (Dordrecht: Reidel), 297
Fruscione, A., McDowell, J. C., Allen, G. E., et al. 2006, Proc. SPIE, 6270, 62701V
Gaspari, M., Brighenti, F., & Temi, P. 2015, A&A, 579, A62
Gaspari, M., McDonald, M., Hamer, S. L., et al. 2018, ApJ, 854, 167
Gaspari, M., Ruszkowski, M., & Oh, S. P. 2013, MNRAS, 432, 3401
Gaspari, M., Ruszkowski, M., & Sharma, P. 2012, ApJ, 746, 94
Gaspari, M., Temi, P., & Brighenti, F. 2017, MNRAS, 466, 677
Gitti, M., Brighenti, F., & McNamara, B. R. 2012, AdAst, 2012, 950641
Gopal-Krishna., & Wiita, P. J. 2000, A&A, 363, 507
Graham, J., Fabian, A. C., & Sanders, J. S. 2008, MNRAS, 386, 278
Hamer, S. L., Edge, A. C., Swinbank, A. M., et al. 2012, MNRAS, 421, 3409
Hamer, S. L., Edge, A. C., Swinbank, A. M., et al. 2014, MNRAS, 437, 862
Hamer, S. L., Edge, A. C., Swinbank, A. M., et al. 2016, MNRAS, 460, 1758
Hansen, L., Norgaard-Nielsen, H. U., & Jorgensen, H. E. 1987, A&AS, 71, 465
Hardcastle, M. J., Massaro, F., & Harris, D. E. 2010, MNRAS, 401, 2697
Hardcastle, M. J., Massaro, F., Harris, D. E., et al. 2012, MNRAS, 424, 1774
Jimenez-Gallardo, A., Massaro, F., Balmaverde, B., et al. 2021, ApJL, 912, L25
Jones, C., Forman, W., Vikhlinin, A., et al. 2002, ApJL, 567, L115
Kauffmann, G., Heckman, T. M., Tremonti, C., et al. 2003, MNRAS, 346, 1055
Kewley, L. J., Groves, B., Kauffmann, G., & Heckman, T. 2006, MNRAS, 372, 961
Kewley, L. J., Heisler, C. A., Dopita, M., et al. 2001, ApJS, 132, 37
Kocevski, D. D., Ebeling, H., Mullis, C. R., et al. 2007, ApJ, 662, 224
Kraft, R. P., Birkinshaw, M., Nulsen, P. E. J., et al. 2012, ApJ, 749, 19
Laing, R. A., Riley, J. M., & Longair, M. S. 1983, MNRAS, 204, 151
Lim, J., Ao, Y., & Dinh-V-Trung. 2008, ApJ, 672, 252
Lynds, R. 1970, ApJL, 159, L151
Madrid, J. P., Chiaberge, M., Floyd, D., et al. 2006, ApJS, 164, 307
Markevitch, M., & Vikhlinin, A. 2007, PhR, 443, 1
Massaro, F., Harris, D. E., & Cheung, C. C. 2011, ApJS, 197, 24
Massaro, F., Harris, D. E., Liuzzo, E., et al. 2015, ApJS, 220, 5
Massaro, F., Tremblay, G. R., Harris, D. E., et al. 2012, ApJS, 203, 31
McCarthy, P. J. 1988, PhD thesis, California Univ. Berkeley
McDonald, M., Veilleux, S., Rupke, D. S. N., et al. 2010, ApJ, 721, 1262
McDonald, M., Veilleux, S., Rupke, D. S. N., et al. 2012, ApJ, 746, 153
McNamara, B. R., Kazemzadeh, F., Rafferty, D. A., et al. 2009, ApJ, 698, 594
McNamara, B. R., & Nulsen, P. E. J. 2007, ARA&A, 45, 117
McNamara, B. R., & Nulsen, P. E. J. 2012, NJPh, 14, 5
McNamara, B. R., Nulsen, P. E. J., Wise, M. W., et al. 2005, Natur, 433, 7021
Nesvadba, N. P. H., Lehnert, M. D., Eisenhauer, F., et al. 2006, ApJ, 650, 693
Nulsen, P. E. J., Hambrick, D. C., McNamara, B. R., et al. 2005b, ApJL, 625, L9
Nulsen, P. E. J., McNamara, B. R., Wise, M. W., et al. 2005a, ApJ, 628, 629
Olivares, V., Salome, P., Combes, F., et al. 2019, A&A, 631, A22
Osterbrock, D. E., & Ferland, G. J. 2006, Astrophysics of Gaseous Nebulae and Active Galactic Nuclei (2nd eda; Sausalito, CA: Science Books)
Pasini, T., Gitti, M., Brighenti, F., et al. 2019, ApJ, 885, 111
Pasini, T., Gitti, M., Brighenti, F., et al. 2021, ApJ, 911, 66
Pizzolato, F., & Soker, N. 2005, ApJ, 632, 821
Prieto, J. L., Krühler, T., Anderson, J. P., et al. 2016, ApJL, 830, L32
Qiu, Y., Bogdanovic, T., Li, Y., McDonald, M., & McNamara, B. R. 2020, NatAs, 4, 900
Qiu, Y., Hu, H., Inayoshi, K., et al. 2021, ApJL, 917, L7
Randall, S. W., Forman, W. R., Giacintucci, S., et al. 2011, ApJ, 726, 86
Randall, S. W., Nulsen, P. E. J., Jones, C., et al. 2015, ApJ, 805, 112
Ricci, F., Lovisari, L., Kraft, R. P., et al. 2018, ApJ, 867, 35
Sanders, R. L., Shapley, A. E., Kriek, M., et al. 2016, ApJL, 825, L23
Shabala, S. S., Ash, S., Alexander, P., & Riley, J. M. 2008, MNRAS, 388, 625
Speranza, G., Balmaverde, B., Capetti, A., et al. 2021, A&A, 653, A150
Spinrad, H., Marr, J., Aguilar, L., & Djorgovski, S. 1985, PASP, 97, 932
Tremblay, G. R., Chiaberge, M., Sparks, W. B., et al. 2009, ApJS, 183, 278
Tremblay, G. R., O'Dea, C. P., Baum, S. A., et al. 2012, MNRAS, 424, 1026
Tremblay, G. R., O'Dea, C. P., Baum, S. A., et al. 2015, MNRAS, 451, 3768
Tremblay, G. R., Oonk, J. B. R., Combes, F., et al. 2016, Natur, 534, 218
Tucker, M. A., Shappee, B. J., Hinkle, J. T., et al. 2021, MNRAS, 506, 6014
Wilman, R. J., Edge, A. C., & Johnstone, R. M. 2005, MNRAS, 359, 755
Zirbel, E. L. 1996, ApJ, 473, 713